Shape optimisation in the design of thin-walled shells as components of aerospace structures

P. A. Suarez Espinoza
suarez@bv.tum.de
K-U. Bletzinger
kub@bv.tum.de
Technische Universität München
Munich, Germany

H. R. E. M. Hörnlein
herbert.hoernlein@eads.com
F. Daoud
fernass.daoud@eads.com
G. Schuhmacher
gerd.schuhmacher@eads.com
EADS
Manching, Germany

M. Klug
markus.klug@premium-aerotec.com
Premium Aerotec
Augsburg, Germany

ABSTRACT

One of the most resent efforts in aircraft design is the replacement of aluminium structures by carbon fibre reinforced polymer composites. Due to lower material and manufacturing costs, doubly curved shapes covering big areas are preferred over simpler surfaces which integrate stiffening profiles. In this context, CAD parameterisation of surfaces allows design solutions by means of classical shape optimisation. Related geometrical parameters are manipulated towards optimal design, generating innovative geometries and detailing.

The presented structure is optimised by reducing the overall weight. The final optimum is guided using stability and strength restrictions in order to assure the safety of the component. Geometrical considerations are also included due to operational reasons. A hierarchical design procedure is developed which results in a work flow from preliminary 'parameter-free' form finding motivated by solving the minimal surface problem. The geometrical model for optimisation is recovered by generating B-Spline surface patches to preserve continuity requirements over large regions. The number of geometrical coefficients are defined by the accuracy in surface generation and the required freedom in surface control. The hierarchical approach reduces the possibilities of ending with an unsatisfactory optimum when several local minima characterise the non-linear problem, as it is usually the case in shape optimal design. A geometrical non-linear analysis is used to verify the performance of the optimum.

Paper No. 3722. Manuscript received 12 May 2011, revised version received 21 November 2011, accepted 25 November 2011.

https://doi.org/10.1017/S0001924000007284 Published online by Cambridge University Press

NOMENCLATURE

Some symbols have two different meanings. A geometrical and a structural definition. Thus, the author tried to keep the usual nomenclature found in the researched literature for each field of study.

a	area of the surface at deformed configuration
a	minimum value of parametric domain
A	area of the surface at undeformed configuration
b	maximum value of parametric domain
c	structural compliance
$C(u)$	free form curve
d	number of data points to be fit to a curve/surface
$\mathbf{e}$	Almansi strain tensor
f	objective function
$\mathbf{F}$	deformation gradient
g_α	covariant base vectors
g	constraint
k	knot multiplicity
$\mathbf{k}^e$	elemental stiffness
$\mathbf{K}$	total stiffness
$\mathbf{K}_e$	linear elastic stiffness
$\mathbf{K}_m$	material stiffness
$\mathbf{K}_g$	geometric stiffness
$\mathbf{K}_l$	external load stiffness
m	total number of all constraints
m_e	total number of equality constraints
m	total number of control points along parametric direction v
n	total number of control points along parametric direction u
n'	total number of control points after a fitting process
$\mathbf{n}$	linking matrix between optimisation and design variables
$\mathbf{N}$	basis functions of geometric representation
$N_{i,p}(u)$	basis function i of degree p along parametric direction u
$N_{j,q}(v)$	basis function j of degree q along parametric direction v
$\mathbf{p}$	applied pressure (vector)
$\mathbf{P}$	curve/surface control points
$P^w_{i,j}$	four-dimensional surface control point
p	applied pressure (module)
$\mathbf{Q}$	points in space to be fit to a curve/surface representation
r	knot values along parametric direction u
$\mathbf{R}$	curve/surface control points
$\mathbf{R}$	residual force vector
$\mathbf{R}_{\mathbf{int}}$	internal forces
$\mathbf{R}_{\mathbf{ext}}$	external forces
s	knot values along parametric direction v
s	optimisation variables
$S(u,v)$	free form surface
t	structural thickness/number of times a knot is inserted or removed
$\mathbf{T}$	induced load imperfection
$\mathbf{u}$	displacement field
u	curve/surface parametric co-ordinate
$\bar{u}_k$	data-parameters in curve
$\mathbf{U}$	knot vector along parametric direction u
v	surface parametric coordinate
$\bar{u}_k$	data-parameters in surface fitting
$\mathbf{V}$	knot vector along parametric direction v
w	weight of control point
$\mathbf{w}$	induced geometric imperfection

https://doi.org/10.1017/S0001924000007284 Published online by Cambridge University Press

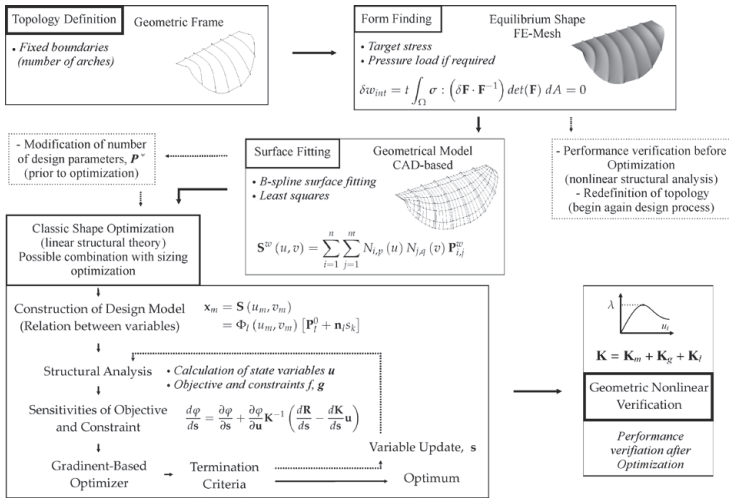


Figure 1. Flow diagram of design process.

w_{int}	internal virtual work
W_{ext}	external virtual work
x	point in space (structural variables)
y	point in space (design variables)
φ	structural response
ϕ	eigenvectors
Φ	basis functions, general representation
λ	load control parameter (load factor)
λ_a	admissible load factor
λ_c	critical load factor
Ω	domain of the system
Ω_σ	boundary of the system
$\boldsymbol{\sigma}$	Cauchy stress tensor at deformed config.
σ_a	admissible stress value
σ_v	von Mises stress at element level
σ_α	principal stresses (in plane)
θ^α	surface co-ordinates

2.0 INTRODUCTION

Manufacturing techniques used in the construction of carbon fibre polymer composites lead to new design concepts regarding structural solutions in the aircraft industry. Due to low material and manufacturing costs approaches like so called black metal designs, which typically end up in stringer stiffened shapes looking very similar to metal structures, loose relevance when choosing a design method. On the other hand sandwich structures with polymer composite skins and a lightweight core are not accepted yet as a suitable solution in the design of big aircraft as they still do not fulfill in-service and fatigue requirements. As an alternative, doubly curved surfaces appear to be a very convenient solution since the associated manufacturing costs do not really differ from the construction of flat panels. Due to the load carrying behaviour of these type of shells consisting mainly in internal tension and compression, the material is more optimally used since bending is reduced. At the same time this property makes possible the integration of adjacent components in a single unit, thus covering bigger areas. Furthermore, the thickness of the shell is allowed to change providing an additional degree of freedom in the design process. Figure 1 shows a diagram including the main stages of the developed design process.

https://doi.org/10.1017/S0001924000007284 Published online by Cambridge University Press

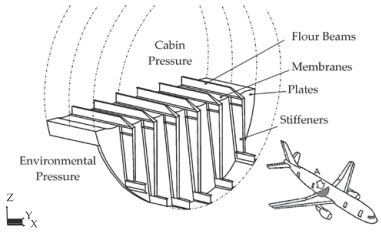


Figure 2. State of the art.

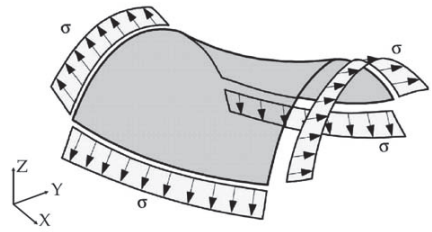


Figure 3. In-plane stress[2].

The first step in the design chain is the use of the form finding technique for geometry generation. Even though this method was born as a design tool for membranes structures[1,2], the generated doubly curved shapes, besides harmonic architecture, provide adequate geometries to be constructed using carbon fiber reinforced polymer composites. Another motivation in using this method is the generation of surfaces of minimal area.

Shape optimal design is proposed to be used after form finding in order to adjust the resulting equilibrium shape to the real external loading and additional geometric considerations. The new geometrical model consisting of a single B-Spline patch provides freedom of shape over the whole structural domain. The number of free parameters that modify the shape during optimisation is defined by the user in such a way so that smooth transitions in shape are possible. Proper surface continuity in the final design is of great advantage for manufacturing purposes.

Since the structural analysis algorithm used in optimisation is derived from the linear theory of solid mechanics, a geometrically nonlinear analysis is necessary afterwards in order to verify the performance of the final optimum. The main reason of this verification is the susceptibility to large displacements and rotations of the analysed structures, due to slenderness of their configuration[3].

The examples shown along this work are presented as a possible solutions to replace the pressurised structural configuration shown in Fig. 2 of a passenger aircraft. This bulkhead, together with the neighboring wing box, define the main landing gear bay, which is subjected to environmental pressure. The passenger cabin is on the other hand artificially pressurised.

2.1 Software and finite elements

Two finite element software were used along this work: (a) CARAT which is being developed at the chair of Structural Analysis at the Technical University of Munich (Germany), was used in form finding calculations and nonlinear simulations; (b) LAGRANGE which is being developed at the department of optimisation in EADS (Manching, Germany), was used for optimisation.

The software CARAT contains a multi-purpose general rotation free element designed for geometrically nonlinear analysis that can be used to model membrane and shell structures[4]. Membrane strains are calculated using isoparametric displacement elements. Bending stiffness can be optionally added where the curvature of the elements is calculated based on the displacements of discrete nodal directors. The bending component uses Kirchhoff theory, avoiding some common locking phenomena associated to Reissner-Mindling bending theory.

The shell finite element used for optimisation is a simplification to curved shells as a combination of plate bending element stiffness and membrane element stiffness. Thus degrees of freedom of both type of elements do not couple. Shear locking is controlled by means of reduced integration[5].

3.0 OVERVIEW OF THE DESIGN PROCESS

The presented design process is divided into five main steps as it is shown in Fig. 1: Topology definition, Form finding, Surface fitting, Classic shape optimisation and Geometric nonlinear verification. Processes inside dis-

https://doi.org/10.1017/S0001924000007284 Published online by Cambridge University Press

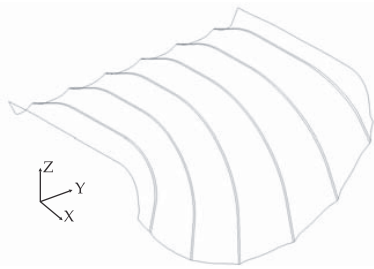


Figure 4. Geometric frame.

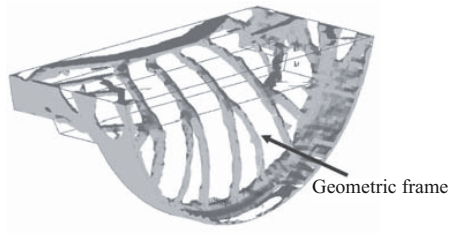


Figure 5. Topological study.

continuous rectangles are possible actions that can be performed if required by the particular example.

Before giving a detailed explanation of each step, a brief overview is presented in the following subsections.

3.1 Topology definition

The definition of the structural topology has to do with the selection of the ribbing pattern before moving to the calculation of single surfaces using form finding. This is done by defining a geometric frame consisting of a certain number of curves in space that become the fix boundary conditions for the calculation of the single surfaces. It corresponds to the outer limits of the whole structure together with the geometry that will enclose the single surfaces as shown in the example of Fig. 4.

Geometric frames calculated throughout this work were obtained using B-Spline curves with the help of CAD-Software (see Fig. 7). One of the guiding parameters used to draw them was the available structural space, as well as the arrangement of adjacent components. The distribution of the central arches was derived from a topological study as explained in Section 4.

3.2 Form finding

Form finding uses the nodal degrees of freedom of an initial FE-mesh to calculate the geometry of the surfaces among the geometric frame. The latter is then used to locate the nodes that will remain fixed during the form finding process. The finer the selected mesh, the more geometrical information is available after form finding. The initial nodal location of the FE-mesh besides the geometric frame is of less importance for the algorithm. The final geometry at the end of the process is called equilibrium shape, since it is the optimal computed shape which is in equilibrium with the target stress. This stress state is the final state to be reached at the end of form finding.

At this stage of the design process, a verification of the performance of the equilibrium surface would be advisable in case the designer is searching for a feasible configuration before optimisation. Adjusting some parameters in form finding or even modifying the structural topology of the component could lead to more convenient configurations. Section 5 compares nonlinear buckling loads of several starting designs. After optimisation is completed, the optimum is once again verified using nonlinear stability analysis as presented in the last section of the paper.

3.3 Surface fitting

The surface fitting algorithm uses the nodal co-ordinates of the equilibrium shape as scattered geometrical data in order to approximate the B-Spline surface, which is used as the geometrical model for optimisation. The location of the resulting geometrical coefficients, also called control points, are free parameters during optimisation.

https://doi.org/10.1017/S0001924000007284 Published online by Cambridge University Press

3.4 Classic shape optimisation

Since form finding considers only membrane loading and boundary conditions in the calculation of doubly curved surfaces, shape optimisation will adjust the initial design to more real physical surroundings. The modification in shape of the thin-walled shell is now dependent on the number and location of the control points, and on further properties of the single B-Spline surface. This is done through the design model, which provides the adequate linking between all present variables (see Section 7.1).

Finally a verification of the optimum is performed by including large displacement and small strains in a final nonlinear static analysis as presented in Section 7.2.

The following sections go through the design process in more detail by using several examples.

4.0 FORM FINDING – TOPOLOGY SELECTION

Form finding is a design methodology for flexible structures such as cables and membranes which have negligible resistance under compression. This type of construction requires a stabilising effect provided by an additional pre-stressed state. Form finding uses this pre-stressed state $\boldsymbol{\sigma}$ as the driving parameter to calculate the structural shape (see Fig. 1). The governing equation of the non-linear problem is given by Ref. 6

$$\boldsymbol{\delta} w_{int} = t \int_{\Omega} \boldsymbol{\sigma} : \left(\boldsymbol{\delta} \mathbf{F} \cdot \mathbf{F}^{-1} \right) det(\mathbf{F})\, dA = 0, \qquad \ldots (1)$$

where $\mathbf{F}$ is the deformation gradient, $\boldsymbol{\sigma}$ the Cauchy stress tensor at the deformed configuration[7], A the area of the surface at the undeformed configuration and t the thickness of the membrane which remains constant during deformation.

In the design of thin-walled shells, form finding is used to generate a suitable geometry which does not need any stabilising forces in service conditions, due to additional bending and compression resistance. Therefore, for this kind of structures, every load present in form finding is not applied in reality. They only control the resulting equilibrium shape and disappear in the later structural analyses.

A prerequisite for the calculation of the equilibrium shape is the definition of the topology of the main frame. The topology decides on the location of additional geometric restrictions during form finding, and influences directly the final shape. Figure 4 shows the geometric frame used in defining the boundary for the calculated surfaces of Fig. 6. The distribution of the central arches was derived from a topological study over a three dimensional region defined by the landing gear bay, which includes the pressurised bulkhead. Figure 5 shows the resulting topology after minimising the structural compliance,

$$c = \frac{1}{2} \int_{\Omega} \boldsymbol{\sigma} : \mathbf{e}\, d\Omega, \qquad \ldots (2)$$

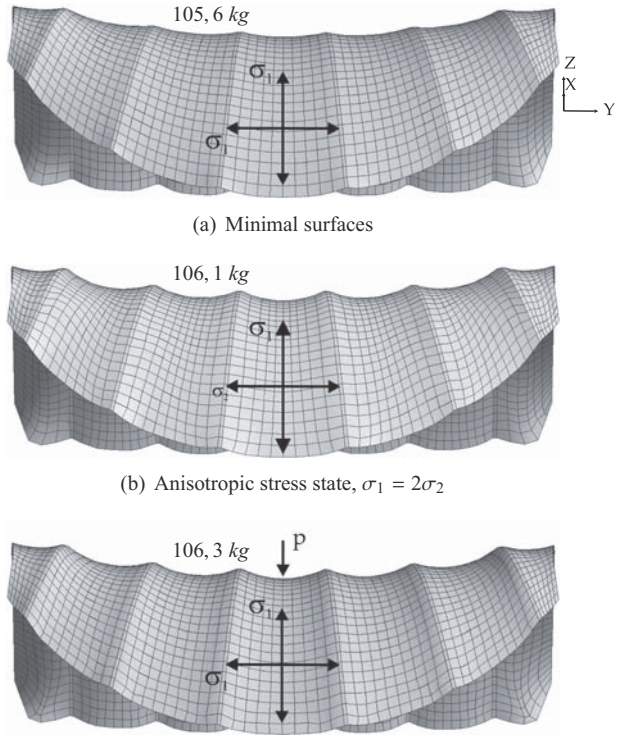
subjected to constant volume. Three dimensional elements were used over the available space, so that the general structural configuration could be identified. The resulting compression arches, which carry the pressure difference, were interpreted as essential component of the geometric frame of the future shell. The new thin-walled structure, besides dividing inner and outer environments, would supply a self stabilising effect when loaded by inner pressure due to tensile and compressive stress trajectories generated thereby.

Figure 7 shows different topologies, modifications in shape and an extension of a six-arch topology, for the same structural component. By observing the load-displacement diagrams of Fig. 7, it can be noted that the critical load could be improved when the shape of the arches was maintained also at the boundaries. After this realisation the bulkhead was extended in order to cover a bigger area with only one structural component. The final number of arches was set to six due to equal number of floor beams at the same location.

4.1 Minimal surfaces

The target stress field $\boldsymbol{\sigma}$ which imposes the final configuration for minimal surfaces has to be homogeneous and isotropic. Figure 6(a) shows the minimal surfaces obtained by applying an isotropic homogeneous stress field to the fixed frame shown in Fig. 4. Variations of minimal surfaces are obtained by providing a different stress field and also by adding normal-to surface loading.

https://doi.org/10.1017/S0001924000007284 Published online by Cambridge University Press



(a) Minimal surfaces

(b) Anisotropic stress state, $\sigma_1 = 2\sigma_2$

(c) Isotropic stress state plus pressure $p = 0.005\sigma_1$.

Figure 6. Form finding on extended concept.

4.2 Anisotropic stress field

An anisotropic stress state is usually addressed when minimal surfaces generate flat shapes with low curvatures, and rather higher curvatures are needed. This is usually the case when boundary modifications are too restrictive. An increment in surface area and structural weight will occur when deviating from minimal surfaces and will depend on the ratio of the principal stresses, $\boldsymbol{\sigma}_1/\boldsymbol{\sigma}_2$. The use of anisotropic stresses is obligatory in cases where a minimal surface is physically not possible to obtain[8].

Figure 6(b) shows the equilibrium surfaces by imposing a stress field in proportion, $\boldsymbol{\sigma}_1 = 2\boldsymbol{\sigma}_2$. $\boldsymbol{\sigma}_1$ and $\boldsymbol{\sigma}_2$ are the in-plane principal stresses.

4.3 Additional loading

In addition to the in-plane stress, other type of external loads could also be included. Due to the normal-to-surface direction of pressure load, it is the only additionally external load that can lead to a final homogeneous stress state, since it does not modify the in-plane stress at the point of application. It rather requires a geometrical modification in order to balance the load in normal direction[6].The additional external virtual work is[6],

$$\begin{aligned} \delta W_{ext}(\mathbf{u}) &= \int_{\partial\Omega_\sigma} \mathbf{p}\cdot\delta\mathbf{u}\,da \\ &= p\int_{\partial\Omega\theta}(\mathbf{g}_1\times\mathbf{g}_2)\cdot\delta\mathbf{u}\,d\theta^1 d\theta^2. \end{aligned} \qquad \ldots (3)$$

https://doi.org/10.1017/S0001924000007284 Published online by Cambridge University Press

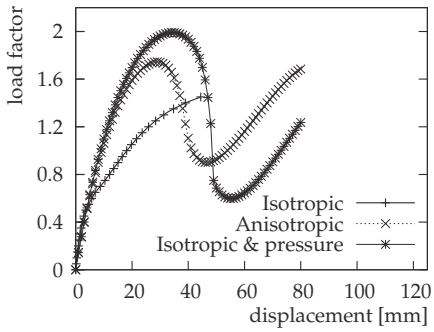


Figure 9. Load-deflection response diagrams.

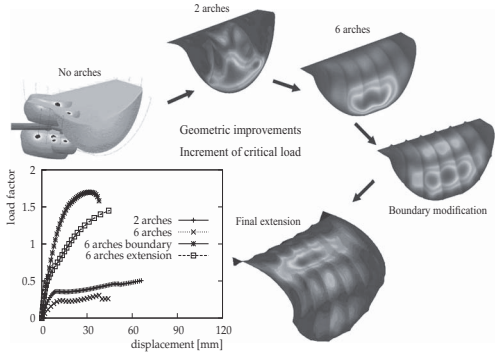
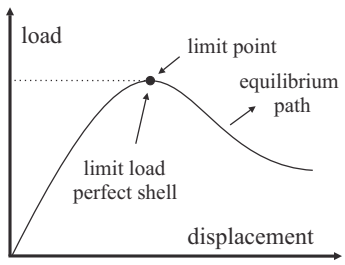
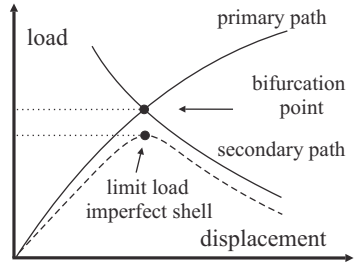


Figure 7. Topological evolution of the frame.



(a) Nonlinear collapse - snapping



(b) Bifurcation buckling - buckling

Figure 8. Buckling modes. Load-deflection response diagrams.

θ^{α} are surface (convective) co-ordinates and g_{α} the covariant base vectors. This additional load is usually used in the design of sinclastic geometries such as inflatable structures[9].

Figure 6(c) shows the calculated equilibrium surfaces for an isotropic homogeneous stress field $\boldsymbol{\sigma}$ and pressure load p in proportion: $p = 0{\cdot}0051\ \boldsymbol{\sigma}_1$.

It can be observed that the curvature of the surfaces along the y axis increases from Figs 6(a) to 6(c). This variation has an impact in the corresponding critical load (see Fig. 9). Each FE-mesh has a total of 3,400 bilinear quadrilateral elements (10,557 dof).

The nonlinear formulation with respect to the unknown parameters $\mathbf{u}$ (Equations 1 and 3) has to be solved using an iteration procedure such as the classical Newton-Raphson method after a suitable linearisation[6]. References 2 and 8 give numerical solutions regarding possible problems of convergence.

5.0 NONLINEAR VERIFICATION – STABILITY ANALYSIS

Thin-walled shells can absorb a significant amount of membrane energy when deformations are kept within acceptable limits. The same amount of energy could also be absorbed by internal bending, whose particular strain mechanism is associated to large deformations. If a thin shell is loaded in such a way that high membrane compression is generated and this stored energy is converted into bending strains, the structure may deform excessively producing unexpected configurations. Conflicts could also be generated for instance with surrounding components, and even the overall structural stability of the system could be endangered. In some cases the deformation may produce sudden movements leading to structural collapse. Figure 8 shows the typical buckling modes which may arise when instability takes place: nonlinear collapse and bifurcation buckling[3].

https://doi.org/10.1017/S0001924000007284 Published online by Cambridge University Press

Table 1
Critical loads

Geometry	Stress in form finding	λc
1.	minimal surfaces $\boldsymbol{\sigma} = \boldsymbol{\sigma} I$	1·5
2.	anisotropic $\sigma_1 = 2\boldsymbol{\sigma}_2$	1·7
3.	isotropic and pressure $p = 0{\cdot}0051\boldsymbol{\sigma}_1$	1·95

Since form finding does not deal with stability problems and the shape optimisation technique applied so far involves only linear deformation theory, nonlinear analysis is used to verify structural performance under more realistic considerations, namely large deformations and small strains. The material model considered in this case is the isotropic perfectly elastic Saint Venant-Kirchhoff material.

The load-deflection history of the structure under analysis, also known as equilibrium path, represents configurations of static equilibrium. It is used to study stability behaviour as the load is being applied by generating load-deflection response diagrams.

The nonlinear stability analysis applied to the different examples shown along this work focuses basically on the location of the first critical point. The corresponding critical load is used as a reference value for shape optimisation, since one of the constrains restricts the linear prebuckling load of the system.

Within the frame of computational modeling using finite elements the equilibrium path is followed using incremental-iterative methods[10]. These numerical methods compute discrete approximations of structural equilibrium, so that the load-deflection history is constructed out of them. The equation used to calculate points along an equilibrium path is given by the residual equation in incremental form[11],

$$\mathbf{R}(\mathbf{u}, \lambda) = \mathbf{R}_{\text{int}}(\mathbf{u}) + \lambda \mathbf{R}_{\text{ext}}(\mathbf{u}) = \mathbf{0} \qquad \ldots (4)$$

where only one load condition, external pressure, is subject to variation. Due to the inclusion of the control parameter as an additional unknown, one more equation has to be included,

$$g(\mathbf{u}, \lambda) = 0 \qquad \ldots (5)$$

This additional constraint can be used to control the increment size ($\Delta\mathbf{u}_n$, $\Delta\lambda_n$) directly or indirectly to enhance robustness and convergence. Examples of this additional constraint can be found in Ref. 10. A consistent linearisation of the equilibrium equations is a pre-requisite for finding a solution using the Newton-Raphson method.

The total stiffness matrix of the system is calculated as the variation of the residual vector with respect to the displacement field,

$$\mathbf{K} = \frac{\partial \mathbf{R}}{\partial \mathbf{u}} = \mathbf{K}_m + \mathbf{K}_g + \mathbf{K}_l. \qquad \ldots (6)$$

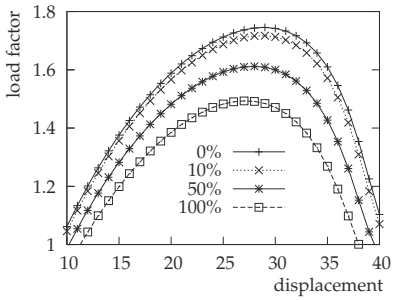
The individual components consist of material, geometric and external load stiffnesses[11-13]. As the tangent stiffness matrix **K** becomes singular along the equilibrium path critical points representing critical loads can be located. Indirect and direct methods to localised critical points while following the equilibrium path can be found in Refs. 10 and 13.

Figure 9 shows load-deflection response diagrams for all three equilibrium surfaces of Fig. 6. The related degree of freedom of each diagram is located at the top of one of the central arches (region of low curvature; see Fig. 10(c)). All three critical loads are larger than 100% of the applied pressure (see Table 1). Nevertheless, the geometry calculated using minimal surfaces experiences a comparatively early material softening.

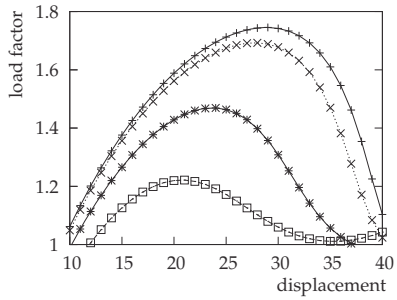
5.1 Imperfection analysis

Imperfections of ideal configurations appear as deviation from perfect parameters and may be of different kind with respect to loads, geometry and material. When structures contain some imperfection they become usually more flexible leading to lower limit loads depending on the distribution of membrane

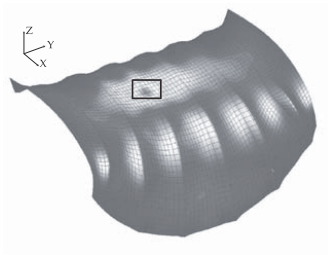
https://doi.org/10.1017/S0001924000007284 Published online by Cambridge University Press



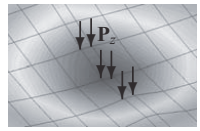
(a) Load imperfection, detail.



(b) Geometric imperfection, detail.

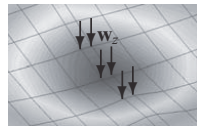


(c) Deformation mode for stimulating imperfections. Nonlinear displacements.



Load imperfection

$6 \times (\| \mathbf{P}_z \| = 600\ N)$.
$\| \mathbf{P}_z \|$= load over one FE
$= 5000\ mm^2 \times 0.12\ \frac{N}{mm^2}$.



Geometric imperfection

$6 \times (\| \mathbf{u}_z \| = 6\ mm)$.
Shell-thickness = 6 *mm*.

(d) Load and geometric induced imperfections over six nodes along the critical arch.

Figure 10. Imperfection analysis on the third equilibrium surface (isotropic stress & pressure).

and bending energy in resisting initial buckling. The first question that arises when trying to reproduce the effects of imperfections is how the imperfection should be represented. It could be for example an induced strain or stress field over a certain area of the structure, or perhaps an initial deformation configuration involving the whole member. In any case, real imperfections are not known in advance, unless they are consequence of a constant failure, for instance within an automatic manufacturing process. One way to analyse the influence of imperfections is to carry out extensive high-quality tests on carefully designed, manufactured and controlled specimens. This is extremely costly and time consuming, particularly when a large number of samples has to be tested to cover a big spectrum of possible situations. A usually more convenient alternative to real tests is to perform numerical simulations on imperfect models.

The strategy used in this paper is to include explicitly in the model, imperfections that may arise during the manufacturing process. As an alternative to explicit method, there are also indirect approaches which are available to the designer (see for instance Ref. 14 where a theoretical indirect method has been selected). Geometric and load imperfections were selected to be included in the following example in order to quantify the impact of imperfections in the modeling. Geometric imperfection is generally one of the first choices to be considered for this kind of structures, where significant deviations in shape can drastically affect the load carrying capacity of the shell. Load imperfection was selected in order to quantify the influence of an additional localised load that could accidentally be experienced during service.

Reference 15 describes three approaches regarding geometrical imperfections for numerical models: realistic, worst and stimulating geometric imperfections[16-18]. Realistic imperfections try to model reality, for instance manufacturing failures. These kind of deficiencies arise usually randomly and there is no way to model them in a deterministic manner, unless the same anomalies appear systematically. The worst imperfection approach searches for the worst imperfection pattern that could affect structural stability. Some studies use the lowest linear eigenmode as the worst imperfection[17]. In case a system presents clustered eigenmodes, a linear combination of them would lead to the worst imperfection pattern[18], and if the prebuckling behavior is highly nonlinear, the worst pattern should include nonlinear eigenmodes[16]. Nevertheless, even single dimple imperfections localised over a small region may be worse than eigenmodes

https://doi.org/10.1017/S0001924000007284 Published online by Cambridge University Press

Table 2
Imperfections of Concept D2. Knock-down factors

% of Imperfection	Load imperfection λ_c	Load imperfection Knock-down factor	Geometric imperfection λ_c	Geometric imperfection Knock-down factor
0	1·74	1·00	1·74	1·00
10	1·72	0·99	1·69	0·97
50	1·61	0·92	1·47	0·84
100	1·49	0·86	1·22	0·70

patterns which involve the whole structure. In any case the, maximum amplitude of the pattern, which is as important as the pattern itself, should be verified. In practice, it is common to use a fraction of the thickness for shell structures[17,18]. Besides all efforts of finding the worst imperfection pattern, its probability of occurring in practice could be very low in the most optimistic case. Simulating geometric imperfection can help to reduce computational costs when a large number of numerical simulations has to be performed, since an equivalent geometric imperfection pattern is chosen to be as simple as possible. This simple pattern should simulate the characteristic physical shell bucking behaviour. Thus, it must have a certain geometric similarity to one of the critical eigenmodes. As it is also the case for worst imperfections, the amplitude of simulating imperfections should be calibrated.

An induced geometric imperfection together with a load induced imperfection are used in the following example (geometry of Fig. 6(b)). Both types of imperfections stimulate the deformation mode at the first limit point over a small area defined by six nodes on the arch that becomes instable as shown in Figs 10(c) and 10(d). The magnitude of each single load was chosen to be the amount of pressure acting over the area of a standard finite element of the corresponding discretisation (area of approx. 5,000mm^2). The magnitude of the applied geometric imperfection was set to be equal to the thickness of the shell.

Table 2 contains critical loads and knock-down factors (ratio of critical loads: between imperfect and perfect structure) for several fractions of the applied imperfections. Knock-down factors are usually used to apply a safety factor to the critical load of a perfect structure. The corresponding load displacement diagrams of the imperfection analysis are shown in Fig. 10.

6.0 GEOMETRICAL MODEL FOR OPTIMISATION

The geometrical model used in shape optimisation is a free form surface, where geometric coefficients $\mathbf{P}_i$ (also known as control points) of the real space $\mathbb{R}^3$ are interpolated with the help of the basis functions ϕ of the parametric space $\mathbb{R}^2$,

$$\mathbf{S}(u,v) = \sum_{i=1}^{n} \Phi_i(u,v)\,\mathbf{P}_i. \qquad \ldots (7)$$

One of the advantages of CAD parameterisations is that they provide a smooth optimal geometry which can also be directly manipulated by CAD-software in case of further modifications and re-optimisation.

Figure 11 shows the mapping of each parametric point (u, v) into the Euclidean space $\mathbf{x}(u,v)$, by using the surface representation $\mathbf{S}(u, v)$. Parameters u and v are real numbers which belong to the closed interval $[a, b]$. The boundaries a and b, may take any positive value which is usually normalised to 0 and 1 respectively.

These surfaces are known as design elements, also called super elements or macro elements since structural finite elements are generated out of them. The surface representation corresponds to the midsurface of the geometrical model used in analysis.

6.1 B-splines

The advantage of using B-splines as the parametric representation for design elements is that the complete shape to be optimised can be modeled using only a single entity. Thus, continuity considerations between several surfaces are no longer needed.

https://doi.org/10.1017/S0001924000007284 Published online by Cambridge University Press

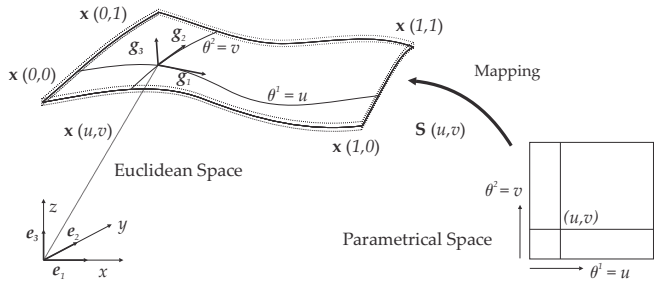


Figure 11. Parametric representation of a surface.

Since B-splines are piecewise polynomials, a local shape control is possible. This control can be modified by refining the network of geometric coefficients and also altering the polynomial degree and knot values. Furthermore, rational B-splines also known as NURBS, are capable of modeling complicated shapes including conic sections.

A general representation of a non-uniform rational B-spline surface ($S^w(u, v) : \mathbb{R}^2 \rightarrow \mathbb{R}^3$) of degree p in the parametric direction u and degree q along the parametric direction v is defined by the following formulation given in homogeneous co-ordinates,

$$\mathbf{S}^w(u,v) = \sum_{i=1}^{n}\sum_{j=1}^{m} N_{i,p}(u)\, N_{j,q}(v)\, \mathbf{P}^w_{i,j}; \quad a \le u, v \le b. \qquad \ldots (8)$$

The components of the four-dimensional control points $\mathbf{P}^w_{i,j}$ are defined as,

$$\mathbf{P}^w_{i,j} = \{xw, yw, zw, w\} \qquad \ldots (9)$$

Control points $\mathbf{P}^w_{i,j}$ in Cartesian co-ordinates are obtained by dividing the first three components by the fourth co-ordinate w, representing the corresponding weight. Weights supply additional control over the shape of the geometrical representation, and are essential for describing conics. Since the fitting algorithm considered in this work does not use weights as variables, they will not be explicitly mentioned in the formulation although the equations include them implicitly. Nevertheless, it is important to mention that modifying their values, besides changes in shape, also produces a distortion of the parametric domain[19].

The piecewise property of a B-spline surface is a consequence of its knot vectors

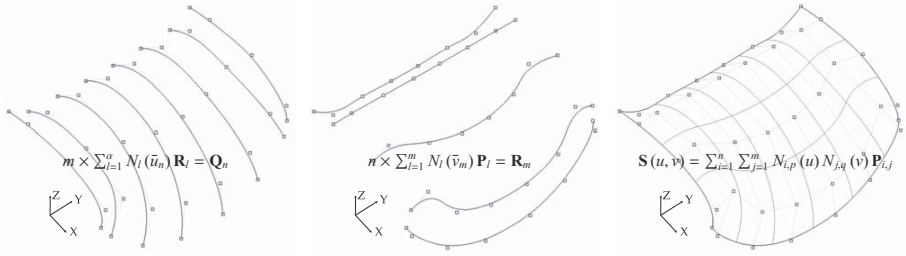
$$\begin{aligned} \mathbf{U} &= \{\underbrace{a,\ldots,a}_{p+1}, u_{p+2},\ldots,u_i,\ldots,u_{r-p-1}, \underbrace{b,\ldots,b}_{p+1}\} \\ \mathbf{V} &= \{\underbrace{a,\ldots,a}_{q+1}, u_{q+2},\ldots,u_i,\ldots,u_{s-q-1}, \underbrace{b,\ldots,b}_{q+1}\}. \end{aligned} \qquad \ldots (10)$$

Knot spans define regions in the parametric domain influenced by the basis function $N_{j,p}$ and $N_{j,q}$ and control points $\mathbf{P}^w_{i,j}$. Therefore modifications of a control point $\mathbf{P}^w_{i,j}$ (or weight $w_{i,j}$) changes the shape of the surface only over the region $[u_i, u_{i+p+1}) \times [v_j, v_{j+q+1})$. Knots may take arbitrary real values along the interval $[a, b]$ with the condition that the subsequent knot should never be smaller than the current one ($u_{i+1} \ge u_i$). Details regarding the mathematical formulation and properties of B-splines and other types of free form surfaces are found in CGAD-related textbooks[19-23].

6.2 Surface fitting

Global B-spline surface approximation of scattered data is the method employed in the developed design process to fit a surface to nodal co-ordinates $\mathbf{Q}_x$. One of the most important tasks is to find a good

https://doi.org/10.1017/S0001924000007284 Published online by Cambridge University Press



(a) Curves u base surface 5×8 (b) Curves v base surface 5×8 (c) Base surface 5×8

Figure 12. Generation of a base surface by bilinear interpolation.

parameterisation for the given data.In our case, data-parameters $\bar{u}_k$ are computed by projection on a base surface as proposed in Ref. 24. The base surface is constructed by means of bilinear curve interpolation[19] over a reduced number of nodal co-ordinates $\mathbf{Q}_y$ ($y << x$) which locations are representative of the total geometry. Other methodologies to calculate data-parameters for surface fitting can be found in Refs. 25-27.

6.2.1. Bilinear interpolation – Base surface

Given a set of data points $\mathbf{Q}_k$ ($k = 1, ..., d$), the problem is to find a set of control points $\mathbf{P}_l$ ($l = 1, ..., n'$), which belong to a curve of degree p having a knot vector $\mathbf{U}$ which interpolates every data point $\mathbf{Q}_k$ ($n' = d$). The system of equations to be solved is given by

$$\sum_{l=1}^{n'} N_l(\bar{u}_k)\,\mathbf{P}_l = \mathbf{Q}_k; \qquad k = 1,...,d; \qquad n' = d. \qquad \ldots (11)$$

In matrix notation: $\mathbf{N} \cdot \mathbf{P} = \mathbf{Q}$,

$$\begin{bmatrix} N_1(\bar{u}_1) & \cdots & N_{n'}(\bar{u}_1) \\ \vdots & \ddots & \vdots \\ N_1(\bar{u}_d) & \cdots & N_{n'}(\bar{u}_d) \end{bmatrix}_{[n' \times n']} \cdot \begin{bmatrix} \mathbf{P}_1 \\ \vdots \\ \mathbf{P}_{n'} \end{bmatrix}_{[n' \times 1]} = \begin{bmatrix} \mathbf{Q}_1 \\ \vdots \\ \mathbf{Q}_d \end{bmatrix}_{[n' \times 1]} \qquad \ldots (12)$$

For curves, the basis functions N_l are equal to $N_{i,p}(\bar{u}_k)$, and for interpolating surfaces N_l takes the form $N_{i,p}(\bar{u}_k)\,N_{j,q}(\bar{v}_k)$.

In order to generate the base surface the selected representative nodes $\mathbf{Q}_y$ are first fitted using a family of curves across the parametric direction u. Finally, the control points of the first family of curves $\mathbf{R}$ are used as new data $\mathbf{Q}_k$ to be fitted along the second parametric direction. For this to be possible, the selected data has to be grid distributed by having n columns and m rows of data ($\mathbf{Q}_y = \mathbf{Q}_{n \times m}$)[19].

One of the fundamental requirements the base surface has to fulfill is a good enough representation of the general shape, taking special care of the boundaries (additional constraints which can be added to formulation 11 can be found in Refs 19 and 28).

The most used parameterisation in B-spline curve fitting and surface fitting of grid data are the uniform, chord length and centripetal methods[28,29]. The chord length method is used in the following example due to satisfactory practical results[19].

The knot vector plays an important role in the quality of the generated geometry, since the stability of the system of equation that has to be solved depends on it. The most common method to compute a suitable knot vector for interpolation of grid data is the technique of averaging suggested in Ref. 30, which gives also good practical results[19,31]. A generalisation of this method where the number of control points approaches the number of data points is proposed in Ref 32.

Figure 12 shows the main stages in the generation of a base surface using bilinear interpolation for the equilibrium surface of Fig. 6(c) after selecting a grid distribution of 5×8 nodes from the FE-mesh. The method is also suitable for irregular meshes.

https://doi.org/10.1017/S0001924000007284 Published online by Cambridge University Press

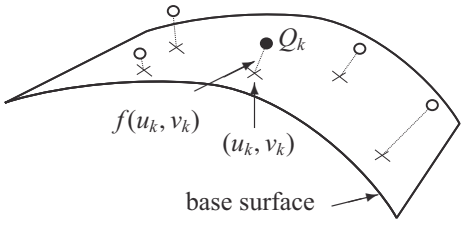


Figure 13. Data projection on base surface.

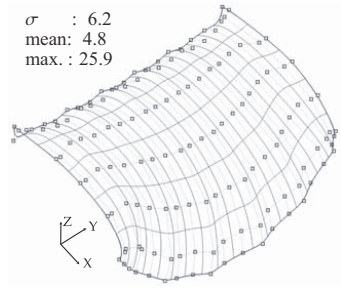


Figure 14. Approximated surface.

6.2.2 Global approximation – Final surface

The least-squares method is the usual solution for fitting a curve or surface to a set of data $\mathbf{Q}_k$ ($k = 1, ..., d$) when the number of geometrical coefficients to be found $\mathbf{P}_l$ ($l = 1, ..., n'$) is smaller compared to the number of scattered data ($d > n'$). The unconstrained minimisation problem takes the form,

$$Min: \quad f(\mathbf{P}_l) = \left\| \mathbf{Q}_k - \sum_{l=1}^{n'} N_l(\bar{u}_k)\,\mathbf{P}_l \right\|^2; \qquad k = 1,...,d. \qquad \ldots (13)$$

After a mathematical rearrangement, taking partial derivatives of f with respect to the unknown geometrical coefficients $\mathbf{P}_l$ and making these results equal to zero, the solution of Equation 13 is obtained by[19]

$$\sum_{l=1}^{n'} N_l(\bar{u}_k)\,N_a(\bar{u}_k)\,\mathbf{P}_l = N_a(\bar{u}_k)\,\mathbf{Q}_k; \qquad k = 1,...,d; \quad a = 1,...,n'. \qquad \ldots (14)$$

In matrix form: $(\mathbf{N}^T \cdot \mathbf{N}) \cdot \mathbf{P} = \mathbf{N}^T \cdot \mathbf{Q}$.

In the previous general formulation n' is equal to $n \cdot m$ for surfaces and equal to n for curves. In the same way the basis functions take the value $N_l = N_{i,p}(\bar{u}_k)\,N_{j,q}(\bar{v}_k)$ for surface approximation and $N_l = N_{i,p}(\bar{u}_k)$ for curve approximation.

Some of the nodal co-ordinates $\mathbf{Q}_k$ can be approximated with higher accuracy by multiplying the corresponding row k with a factor bigger than one in Equation 13, as it would be the case for boundary nodes.

Parameters $\bar{u}_k$ and $\bar{v}_k$ assigned to each data Q_k are calculated by projecting each node onto the base surface (see Fig. 13). Thus, the parametric point $(\bar{u}_k, \bar{v}_k)$ is computed by solving an unconstrained minimisation problem where the objective function $f(u,v)$ is given by the distance between the selected data Q_k and the related point on the surface $\mathbf{S}(u,v)$[33],

$$Min: \quad f(u,v) = \frac{1}{2}\left\| \mathbf{S}(u,v) - \mathbf{Q}_k \right\|^2. \qquad \ldots (15)$$

The minimum of the function f is obtained by taking its partial derivatives *w. r. t.* the free parameters u and v and making these expressions equal to zero. Thus, the following nonlinear partial differential equations have to be solved by using for instance the Newton-Raphson method after a suitable linearisation,

$$f(u,v)_{,u} = (\mathbf{S}(u,v) - \mathbf{Q}_k) \cdot \mathbf{S}(u,v)_{,u} = 0$$
$$f(u,v)_{,v} = (\mathbf{S}(u,v) - \mathbf{Q}_k) \cdot \mathbf{S}(u,v)_{,v} = 0 \qquad \ldots (16)$$

In general, for fitting purposes the knot values have higher freedom of selection compared to parameter values, so that they can be perturbed without causing numerical problems[34]. Nevertheless, they also have an influence on the final shape. One common solution is to use an open uniform knot vector.The degree of approximation of the fitted surface will also depend on the number of control points which are set by the user. The quantity of geometrical coefficients of a geometrical model for shape optimisation will be decided according to the compromise between two fundamental requirements: (a) enough geometrical freedom in order to generate a suitable number of possible feasible configurations, and (b) a lower prob-

https://doi.org/10.1017/S0001924000007284 Published online by Cambridge University Press

ability of having numerical drawbacks in mathematical optimisation by decreasing the number of excessive design variables.

The surface shown in Fig. 14 is used as a geometrical model in the subsequent shape optimisation examples. This approximated surface was generated using a base surface containing the same number of control points. The boundary nodes were set to be more relevant to the fitting algorithm by multiplying the related equations by a factor of five in formulation 13.

6.3 Modification in the number of geometrical coefficients

It might be necessary to modify geometrical flexibility in some regions of the geometrical model either before any optimal shape has been obtained or in order to begin with a new optimisation. This can be reached by increasing or decreasing the number of design parameters $\mathbf{P}_{i,j}$ at certain locations providing a different degree for shape control in the optimisation process. This modification is possible when knots are added or removed from the initial knot vectors. In case the number of design parameters has to be increased uniformly over the entire domain, a second global surface fitting should be performed anew.

6.3.1 Knot insertion

B-splines do not have any limitation in the number of control points while having the same polynomial degree. The number is increased by adding knots without affecting the geometrical shape. Since the number of control points is directly related to the number of knots, adding the knot $\bar{u}_t$ times increases the number of control points (and related B-spline functions) in t as well.

In case of curves, the new control points are obtained by comparing initial and final representations $\mathbf{C}(u)^w = \bar{\mathbf{C}}(u)^w$,

$$\sum_{i=1}^{n} N_{i,p}(u)\,\mathbf{P}_i^w = \sum_{i=1}^{n+t} \bar{N}_{i,p}(u)\,\bar{\mathbf{P}}_i^w. \qquad \ldots (17)$$

In case of inserting a knot into a surface $\mathbf{S}(u,v)^w$, Equation 17 has to be solved for each row or column of control points respectively. More details on how to solve 17 are found in Refs. 19 and 35.

The new knot to be inserted can also have the value of an already existing knot. As a consequence the initial knot multiplicity is increased whereas the continuity of the representation decreases at the corresponding location. At a knot value of multiplicity k, the curve (or surface in the corresponding parametric direction) is C^{p-k} continuous. In the interior of knot spans the geometrical representation remains C^{p-1} continuous.

Figure 15 shows an example of knot insertion. The new knots 0·3 and 0·7 are inserted into the knot vector $\mathbf{U} = \{0, 0, 0, 0{\cdot}2, 0.4, 0{\cdot}6, 0{\cdot}8, 1, 1, 1\}$ of a surface approximation over the equilibrium shape of Fig. 6(b). It can be observed that the geometry is not modified, since new control points lie on the initial control polygon. In each insertion, one row of control points is replaced by two new rows. The approximated surface has a polynomial degree equal to two in both directions.

6.3.2 Knot removal

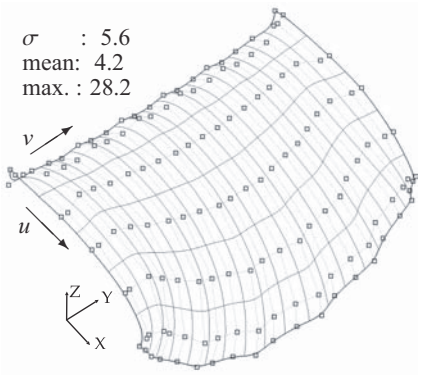
Knot removal deletes a knot $\bar{u}$ from an existing knot vector **U.** Practically all interior knots could be removed from a knot vector, if no care is given to shape deviations. Therefore, a modification of the initial geometry is usually restricted to a user defined tolerance that measures geometrical deviations on the parametric domain. In case a knot which was previously inserted into a B-spline entity is subsequently removed there are no modifications in the geometry.

For rational B-spline curves, the new control points are obtained by comparing initial and final representations,

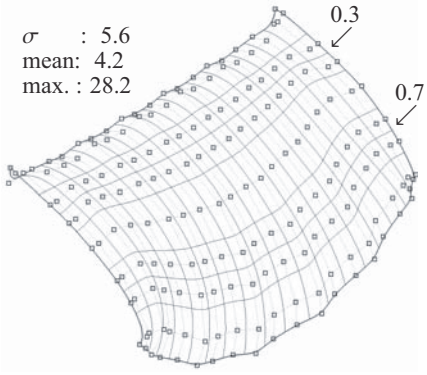
$$\sum_{i=1}^{n} N_{i,p}(u)\,\mathbf{P}_i^w = \sum_{i=1}^{n-t} \bar{N}_{i,p}(u)\,\bar{\mathbf{P}}_i^w. \qquad \ldots (18)$$

In case of removing a knot from a surface $\mathbf{S}(u, v)^w$, Equation 18 has to be solved for each row or column of control points. More details on how to solve Equation 18 are found in Refs 19, 35.

https://doi.org/10.1017/S0001924000007284 Published online by Cambridge University Press

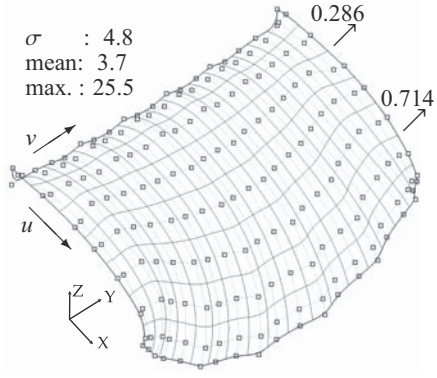


(a) Approximated surface, 20x7 CP

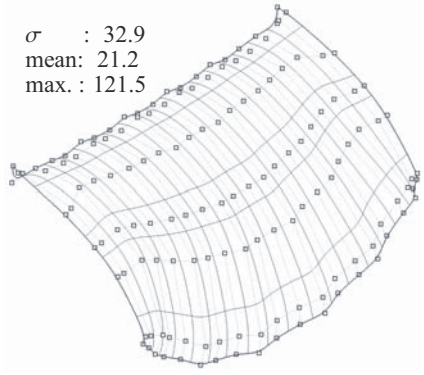


(b) Two knots inserted. New surface of 20x9 CP

Figure 15. Knot insertion. Comparison between errors.



(a) Approximated surface, 20x9 CP



(b) Two knots removed. New surface of 20x7 CP

Figure 16. Knot removal. Comparison between errors.

Figure 16 shows the geometrical modifications of a B-spline surface after the knots 0·286 and 0.714 are removed from the knot vector $\mathbf{U} = \{0, 0, 0, 0{\cdot}143, 0{\cdot}286, 0{\cdot}428, 0{\cdot}571, 0{\cdot}714, 0{\cdot}857, 1, 1, 1\}$. The affected surface is the result of using surface fitting on the equilibrium shape shown in Fig. 6b. Each time a knot was removed a new row of control points replaced two old ones. Geometrical modifications are evident in this example.

7.0 SHAPE OPTIMISATION

The mathematical formulation of a general optimisation problem takes the form

$$\begin{array}{lll} \textit{minimize}: & f(\mathbf{s}); & \mathbf{s} \in \mathbb{R}^n \\ \textit{subject to}: & g_j(\mathbf{s}) = 0; & j = 1, ..., m_e \\ & g_j(\mathbf{s}) \leqslant 0; & j = m_e + 1, ..., m \\ & \mathbf{s}_l \leqslant \mathbf{s} \leqslant \mathbf{s}_u & \end{array} \quad \ldots (19)$$

where f is the objective function and $\mathbf{g}$ equality and inequality constraints. m_e is the number of equality constraints, and m stands for the total number of constraints. The optimal combination of independent variables s gives the minimum value of the objective function and at the same time fulfills the given constraints. The restrictions for upper and lower limits (bound restrictions $\mathbf{s}_l$ and $\mathbf{s}_u$ respectively) imposed on the variables are also known as side- or gage-constraints.

https://doi.org/10.1017/S0001924000007284 Published online by Cambridge University Press

In our case, the objective function $f(\mathbf{s})$ to be minimised is the total structural weight. Two inequality constraints are considered. The first one restricts the maximum value of the von Mises stress at element level,

$$g_{\sigma_v} = \frac{\boldsymbol{\sigma}_v}{\boldsymbol{\sigma}_a} - 1 \leq 0, \quad \ldots (20)$$

$$\sigma_v = \sqrt{\sigma_x^2 + \sigma_y^2 - \sigma_x \sigma_y + 3\tau_{xy}^2}. \quad \ldots (21)$$

The second one imposes a limit for the lowest structural eigenvalue

$$g_{\lambda} = \frac{\boldsymbol{\lambda}}{\boldsymbol{\lambda}_a} - 1 \leq 0, \quad \ldots (22)$$

calculated by means of linearised prebuckling,

$$(\mathbf{K}_e + \lambda \mathbf{K}_g)\boldsymbol{\phi} = 0 \quad \ldots (23)$$

Linearised prebuckling is a commonly used method which localises directly critical points without being concerned with the task of tracing equilibrium paths up to these points. This is possible, since the stiffness matrix **K** is considered to be linearly influenced by the displacement field **u**. Even though this assumption is not completely valid for the analysed type of structures, the critical load provided by linearised prebuckling is a good reference value in several cases and the simplicity of the methodology is well suitable for optimisation. Nevertheless, a verification of the optimum using a nonlinear formulation is mandatory for safety reasons. Besides considering the influence of the pressure load in the total stiffness, a geometrical nonlinear simulation can predict more accurate results when dealing with imperfections (see Section 5.1).

Sensitivities of objective and constraints are the fundamental information which a gradient based optimiser requires in order to calculate each subsequent combination of improved optimisation variables **s**. The usual strategy to calculate sensitivities in shape optimisation problems is the semi-analytical method[36].

The sensitivities of any structural response φ which in general also depends on the displacement field **u** are obtained by taking total derivatives,

$$\frac{d\varphi}{d\mathbf{s}} = \frac{\partial \varphi}{\partial \mathbf{s}} + \frac{\partial \varphi}{\partial \mathbf{u}} \frac{d\mathbf{u}}{d\mathbf{s}}. \quad \ldots (24)$$

Equation 24 includes an explicit part which is usually easy to obtain or equal to zero and an implicit part through the dependence of **u**. The total derivatives d**u**/d**s** have to be calculated using the discretised formulation of equilibrium equations, which are in this case linear about the displacement field **u**,

$$\mathbf{K}\mathbf{u} = \mathbf{R}_{ext};\ \mathbf{u} = \mathbf{K}^{-1}\mathbf{R}_{ext}. \quad \ldots (25)$$

Taking derivatives with respect to **s**, and solving for d**u**/d**s**, the following expression is obtained,

$$\frac{d\mathbf{u}}{d\mathbf{s}} = \mathbf{K}^{-1}\left(\frac{d\mathbf{R}}{d\mathbf{s}} - \frac{d\mathbf{K}}{d\mathbf{s}}\mathbf{u}\right). \quad \ldots (26)$$

Equation 24 is solved using either the adjoint or direct approach depending on the relative number of load cases, constraints and optimisation variables[36].

Sensitivities of the load vector $\mathbf{R}_{ext}$ and stiffness matrix **K** are then calculated using finite differences at element level. The load vector $\mathbf{R}_{ext}$ is usually considered to be independent of **s**, so that its sensitivities are set to be zero. The sensitivities of the stiffness matrix is obtained by:

$$\frac{d\mathbf{K}}{d\mathbf{s}} = \sum_{i=1}^{nelem} \frac{d\mathbf{k}_i^e}{d\mathbf{s}} \approx \sum_{i=1}^{nelem} \frac{\Delta \mathbf{k}_i^e}{\Delta \mathbf{s}}. \quad \ldots (27)$$

https://doi.org/10.1017/S0001924000007284 Published online by Cambridge University Press

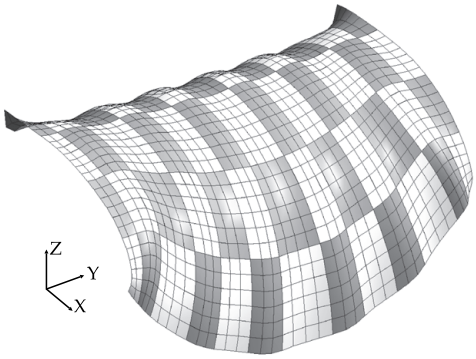


Figure 17. Distribution of sizing variables. FE-mesh for optimisation.

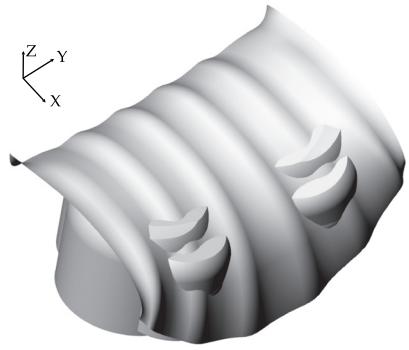


Figure 18. Geometrical restriction.

The number of elements *nelem* considered in Equation 27 varies with each optimisation variable and depends on how many design variables are linked to the current optimisation variable. When using a B-Spline as geometrical model the selected finite elements are the ones affected by the region $[u_i, u_{i+p+1}) \times [v_j, v_{j+q+1})$ of every linked design variable $\mathbf{P}_{i,j}$ (see Section 6.1). For a better understanding of the previously mentioned variable linking see Section 7.1.

There is a source of error associated to shape optimisation which increases with mesh refinement. It arises with respect to the rigid body rotation behaviour of the approximated stiffness matrix derivative[37]. The finite elements that are affected are the ones which stiffness depends on different powers of the independent variables as it is the case of elements including bending stiffness[36]. There exist several solutions to the problem[37]. The examples shown later were calculated using central difference approximation of the stiffness matrix. In Ref. 37, a method for the computation of correction factors based on product spaces of rigid body rotation vectors is presented, where the element stiffness matrix is modified by this factors in order to obtain 'exact' sensitivities.

7.1 Variable linking

In the context of shape optimisation using CAD-based design elements, there is a relation between three different kinds of variables: optimisation, design and structural variables (**s**, **y** and **x** respectively). They are linked to each other in the following way:

$$\begin{aligned} \mathbf{x}_m = \mathbf{S}\left(u_m, v_m\right) &= \mathbf{\Phi}_l\left(u_m, v_m\right)\mathbf{y}_l \\ &= \mathbf{\Phi}_l\left(u_m, v_m\right)\left[\mathbf{P}_l^0 + \mathbf{n}_l s_k\right]. \end{aligned} \quad \ldots (28)$$

Variables **y** are a linear combination of **s**, and **x** are a linear combination of **y**. $\mathbf{n}_l$ constitute the linking matrix of linear relations between optimisation and design variables. Vectors $\mathbf{n}_l$ could represent for instance pre-defined moving directions, symmetric/antimetric considerations as well as linear combinations. Φ_l are the basis functions of the free form surface and establish linear relations between structural and design variables (see Equation 8). Finally, u_m and v_m are the surface parameters associated to the structural variable x_m, which are the nodal co-ordinates of the finite element mesh.

7.2 Optimisation results – nonlinear verification

The stress constraint considers an allowable value for the von Mises stress criteria equal to 200N/mm^2, whereas the stability constraint sets a limit value for the critical load factor equal to 3·0. Sensitivities were calculated using a step size for optimisation variables equal to $1 \times 10E-6$. The optimisation method used was the well-known sequential quadratic programming[38].

https://doi.org/10.1017/S0001924000007284 Published online by Cambridge University Press



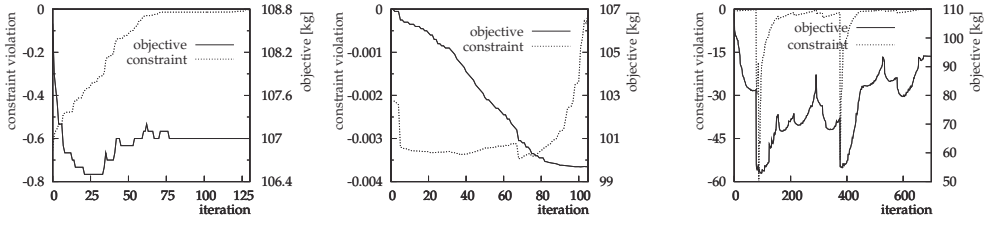
(a) View 1 (b) View 2 (c) Load-displacement diagrams.

Figure 19. Optimal configuration by using 28 optimisation variables for shape control. Shape and subsequent sizing.



(a) View 1 (b) View 2 (c) Load-displacement diagram.

Figure 20. Optimal configuration by using 28 optimisation variables for shape control. Shape combined with sizing.



(a) Shape Optimization (b) Subsequent Sizing Optimizaion (c) Simultaneous Shape and Sizing Optimization

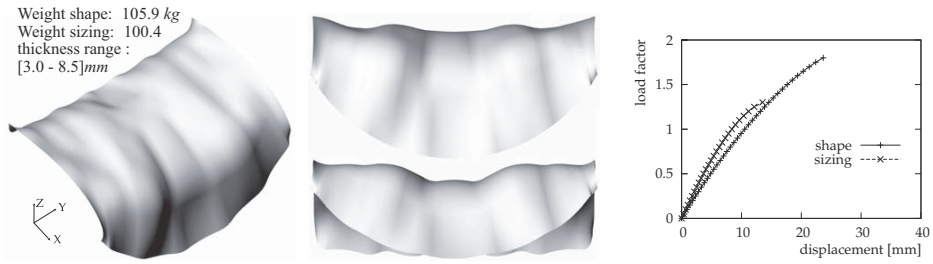
Figure 21. Objective function and constraint violation during optimisation – 28 optimisation variables for shape control.

Figure 17 shows the *FE*-mesh generated from the B-spline surface of Fig. 14 consisting of 1,000 bilinear quadrilateral elements (6,396 dof). The same figure shows the areas assigned to sizing variables. These areas usually concentrate compression (arches regions) and tension (surfaces regions) stresses due to the kind of applied load. Along the y axis a number of four divisions was set to differentiate between boundary and inner regions. A total of 28 sizing variables is left after symmetric linking. The initial thickness was equal to 6mm.

Figure 18 shows the geometrical conflict between the landing gear and the bulkhead after form finding. This problem was solved by moving the corresponding control points out of the area of conflict following their own directions of movement for optimisation until both geometries intersected. Before optimisation the lower boundaries of the affected control points were set to zero.

All numerical examples use the same geometrical model shown in Fig. 14 which has 140 design parameters. Excluding all 50 boundary parameters, the remaining 90 were used as design variables. Finally,

https://doi.org/10.1017/S0001924000007284 Published online by Cambridge University Press



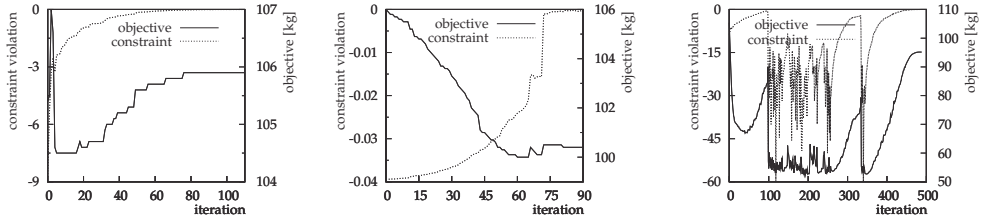
(a) View 1 (b) View 2 (c) Load-displacement diagrams.

Figure 22. Optimal configuration by using 35 optimisation variables for shape control. Shape and subsequent sizing.



(a) View 1 (b) View 2 (c) Load-displacement diagram.

Figure 23. Optimal configuration by using 35 optimisation variables for shape control. Shape combined with sizing.



(a) Shape Optimization (b) Subsequent Sizing Optimizaion (c) Simultaneous Shape and Sizing Optimization

Figure 24. Objective function and constraint violation during optimisation – 35 optimisation variables for shape control.

by using symmetric linking with respect to the *xz* plane and connecting two design variables to one optimisation variable for all central surfaces along each row of control points, a total of 35 independent optimisation variables are left. Nevertheless, the number of optimisation variables is not the same in all cases. The following results were obtained after optimising two examples, which make use of 28 and 35 optimisation variables respectively. The optimal shapes of Figs 19 and 20 were calculated using 28 optimisation variables, since the third row of geometrical coefficients (*u* constant) was set to be fixed during optimisation, in order to maintaining the initial structural topology during optimisation. For the same reason the geometrical coefficients were only allowed to move in *x* and *z* directions. On the other hand, the final optima of Figs 22 and 23 were computed by using all previously mentioned 35 optimisation variables. In this case, a higher freedom of shape generation was provided by using as direction of movement the normal to surface direction at each control point. This direction was updated at every optimisation step.

For the sake of simplicity, load-displacement diagrams are displayed until the first critical point was found. Figures 19(c), 20(c), 22(c) and 23(c) show the results of non-linear structural analyses of the optimised configurations as a verification of structural performance. Even though in some optimal config-

https://doi.org/10.1017/S0001924000007284 Published online by Cambridge University Press

urations the critical load was drastically reduced, specially the final optima obtained by combining shape and sizing variables, all of them represent feasible solutions. The value of the von Mises stress in the nonlinear analyses are within limits for a load factor equal to 1·0 in each case.

Figures 21 and 24 show the values of objective function and constraint violation during each optimisation process. By combining shape and sizing variables, the optimisation algorithm (SQP) restarted several times the calculation by using a different set of optimisation variables. In all cases the termination criterion to stop the optimisation was the solution of the the Kuhn-Tucker conditions[36] using an accuracy of 1*E*-6. This criterion was met only for sizing optimisation. Optimisation using shape variables were stopped after a reasonable value for the constraint violation was reached.

8.0 CONCLUSIONS

Differences between critical loads obtained by means of linear and nonlinear deformation theories over the same structural configuration are significant, due to the load carrying behaviour characterised by large displacements. Other important contribution to this effect might be produced by the difference in FE-formulations and software used for each case. It is important to notice that the optimal configurations obtained using only shape variables provide the highest critical loads.

The fitting algorithm used to generate the geometrical model does not consider symmetry conditions for the distribution of control points. This situation leads to differences of about 10mm in terms of location of symmetric control points (example shown in Fig. 14). Such deviations were considered as a geometrical imperfection. Nevertheless, an imperfection analysis of any optimal configuration, as the one shown in Section 5.1, would be strongly recommended for safety reasons.

There are still some improvements that can be implemented in the optimisation process in order to increase the quality of results. For instance, update of the force direction after every optimisation step, the calculation of the sensitivities of the load vector for the sensitivity analysis, as well as the inclusion of a suitable geometric constraint. Regarding sizing optimisation a smoothing algorithm that controls the thickness size of adjacent regions would also help to improve the quality of the results. A second B-Spline surface controlling only the element thickness could be a good alternative in this case.

It could be observed from the examples shown in section 4 that form finding is a design tool that generates smooth and elegant shapes in the design of thin-walled structures and provides good structural qualities for the load carrying capacity of shells.

Once again it was demonstrated that classical shape optimisation gives the designer the possibility of generating innovative solutions that fulfil the imposed restrictions.

Finally, by observing the final results it can be concluded that the developed design process was successfully applied to the presented example.

REFERENCES

1. BLETZINGER, K.U. and WÜCHNER, R. Form- Trägt - Formfindung vorgespannter Membrantragwerke, 2004, Dresdner Baustatik Seminar - Kreative Ideen im Ingenieurbau, **8**, Dresden, Germany.
2. WÜCHNER, R. Mechanik und Numerik der Formfindung und Fluid- Struktur-Interaktion von Membrantragwerken; 2007, PhD thesis; Technische Universität München, Germany.
3. BUSHNELL, D. *Computerized buckling analysis of shells*, 1989, Kluwer Academic Publishers.
4. LINHARD, J., WÜCHNER, R. and BLETZINGER, K.U. Membranes to shells the ceg rotation free shell element and its application in structural analysis, *Finite Elements in Analysis and Design*, 2007, **44**, pp 63–74.
5. HUGHES, T. *The Finite Element Method: Linear Static and Dynamic Finite Element Analysis*, 2000, Dover Publication.
6. BLETZINGER, K.U and, RAMM, E. A General finite element approach to the form finding of tensile structures by the updated reference Strategy, *Int J of Space Structures,* 1999, **14**, (2), pp 131–145.
7. HOLZAPFEL, G. *Nonlinear Solid Mechanics*, 2000, John Wiley & Sons, Chichester: UK.
8. LINHARD, J. Numerisch-mechanische Betrachtung des Entwurfsprozesses von Membrantragwerken, 2009, PhD thesis, Technische Universität München, Germany.
9. JARASJARUNKIAT, A. Nonlinear Analysis of Pneumatic Membranes From Subgrid to Interface, 2009, PhD thesis; Technische Universität München, Germany.
10. WRIGGERS, P. *Nichtlineare Finite-Element-Methoden*, 2001, Springer- Verlag, Berlin, Germany.
11. BELYTSCHKO, T., LIU, W. and MORAN, B. *Nonlinear Finite Elements for Continua and Structures*, 2000, John Wiley & Sons, Chichester, UK.

https://doi.org/10.1017/S0001924000007284 Published online by Cambridge University Press

12. RIKS, E. Some computational aspects of the stability analysis of nonlinear structures, *Computer Methods in Applied Mech and Eng,* 1984, **47**, pp 219–259.
13. REITINGER, R. Stabilität und Optimierung imperfektionsempfindlicher Tragwerke, 1994, PhD thesis, Institut für Baustatik der Universität Stuttgart, Germany.
14. PONTOW, J. and DINKLER, D. Impefection sensitivity and limit loads of spherical shells under radial pressure, PAMM Proc, *Appl Mech*, 2005, **5**, pp 253–254, Wiley-VCH Verlag. Weinheim; Germany.
15. SCHMIDT, H.. Stability of steel shell structures general report, *J Constructional Steel Research,* 2000, **55**, pp 159–181.
16. LU, Z., OBRECHT, H. and WUNDERLICH, W. Imperfection sensitivity of elastic and elastic-plastic torispherical pressure vessel heads, *Thin-Walled Structures*, 1995, **23**, pp 21–39.
17. NEMETH, M.P., BRITT, V.O., COLLINS, T.J. and STARNES, J.H. Nonlinear analysis of the space shuttle superlightweight external fuel tank, 1996, Technical Report 3616, National Aeronautics and Space Administration, Langley Research Center, Hampton, VA, USA.
18. NEMETH, M.P., YOUNG, R.D., COLLINS, T.J. and STARNES, J.H. Effects of initial geometric imperfections on the non-linear response of the space shuttle superlightweight liquid-oxygen tank, *Int J Non-linear Mech*, 2002, **37**, pp 723–744.
19. PIEGL, L. and TILLER, W. *The NURBS Book*, 1997, Springer-Verlag, Berlin, Germany.
20. FARIN, G. *NURBS*, 1999, Peters.
21. FARIN, G. *Curves and Surfaces for CAGD: a Practical Guide*, 2002, Fifth edition, Morgan Kaufmann.
22. COHEN, E., RIESENFELD, R.F. and ELBER, G. *Geometric Modeling with Splines*, 2001, A K Peters.
23. ROGERS, D.F. *An Introduction to NURBS*, 2001, Morgan Kaufmann.
24. MA, W. and KURTH, J. Parameterization of randomly measured points for least squares fitting of b-spline curves and surfaces, *Computer Aided Design,* 1995, **27**, (9), pp 663–675.
25. HORMANN, K. Fitting free form surfaces, *Principles of 3D Image Analysis and Synthesis*, 2000, International Series in Engineering and Computer Science, **556**, Kluwer Academic Publishers, Boston, MA, USA.
26. HORMANN, K. From scattered samples to smooth surfaces, *Proceedings of Geometric Modeling and Computer Graphics,* 2003.
27. SINTEF, M.F. and FLOATER, M.S. Meshless parameterization and b-spline surface approximation, *The Mathematics of Surfaces IX*, 2000.
28. PIEGL, L.A. and TILLER, W. Curve interpolation wiht arbitrary end derivatives, *Engineering with Computers*, 2000, **16**, pp 73–79.
29. SHAMSUDDIN, S., AHMED, M. and SAMIAN, Y. Nurbs skinning surface for ship hull design based on new parameterization method, *Int J Manuf Technology*, 2006, **28**, pp 936–941.
30. DE BOOR, C. *A Practical Guide to Splines*, 1978, New York, Springer-Verlag.
31. TOKUYAMA, Y. Skinning-surface generation based on spine-curve control, *The Visual Computer*, 2000, **16**, pp 134–140.
32. PIEGL, L.A. and TILLER, W. Least-squares b-spline curve approximation with arbitrary end derivatives. *Engineering with Computers*, 2000, **16**, pp 109–116.
33. SCHUHMACHER, G. Multidisziplinäre, fertigungsgerechte Optimierung von Faservebund-Flchentragwerken, 1995 , PhD thesis, Fachbereich Maschinentechnik der Universität-Gesamthochschule Siegen.
34. PIEGL, L.A. and TILLER, W. Surface approximation to scanned data methods in applied mechanics and engineering, *The Visual Computer*, 2000, **16**, pp 386–395.
35. LYCHE, T. *Knot insertion and Deletion Algorithms for B-spline Curves and Surfaces*, 1993.
36. HAFTKA, R. and GÜRDAL, Z. *Elements of Structural Optimization*, 1992, Kluwer Academic Publishers, Dordrecht, The Netherlands.
37. BLETZINGER, K.U., FIRL, M. and DAOUD, F. Approximation of derivatives in semi-analytical structural optimization, *Computers & Structures*, 2008, **86**, pp 1404–1416.
38. SCHITTKOWSKI, K. On the convergence of a sequential quadratic programming method with an augmented lagrangian line search function, *Operationsforschung und Statistik, Ser Optimization*, 1983, **14**, (2), pp 197–216.

https://doi.org/10.1017/S0001924000007284 Published online by Cambridge University Press